American Mineralogist, Volume 96, pages 1537–1546, 2011

Raman spectroscopy of titanomagnetites: Calibration of the intensity of Raman peaks as a sensitive indicator for their Ti content

Pavel Zinin,[1,*] Lisa Tatsumi-Petrochilos,[2] Lydie Bonal,[1] Tayro Acosta,[1] Julia Hammer,[2] Stuart Gilder,[3] and Mike Fuller[1]

[1]Hawaii Institute of Geophysics and Planetology, Honolulu, Hawaii 96822, U.S.A.
[2]Department of Geology and Geophysics, University of Hawaii, Honolulu, Hawaii 96822, U.S.A.
[3]Department of Earth and Environmental Sciences-Geophysics, Munich University, Munich 80333, Germany

Abstract

A systematic study of the Raman spectra of the titanomagnetite solid-solution series ($Fe_{3-x}Ti_xO_4$) for x = ~0.0, 0.2, 0.4, and 0.6 has been conducted. The samples showed combinations of five previously predicted Raman peaks at ~190, 310, 460, 540, and 670 cm^{-1} that correspond to vibrational modes with $T_{2g}(1)$, E_g, $T_{2g}(3)$, $T_{2g}(2)$, and A_{1g}, respectively. The calibration of Raman spectra for titanomagnetite with known values of Ti concentrations reveals a strong dependence of relative intensity for the $T_{2g}(2)$ and $T_{2g}(3)$ modes on Ti concentration. The most prominent feature is the appearance and increase in the relative intensity of a $T_{2g}(3)$ peak above x = ~0.2. On the other hand, the Raman peak for the $T_{2g}(2)$ mode gradually diminishes as Ti increases and nearly disappears at x = ~0.6. Combining the two relative intensities potentially provides a sensitive indicator of Ti content. The technique was applied to study titanomagnetite in grains from Hana Volcanics and melatroctolite from Rhode Island.

Keywords: Titanomagnetites, Raman spectroscopy, Fe-Ti oxides, spinel

Introduction

Iron-titanium oxide minerals are fundamental to paleo, rock, and environmental magnetic studies because they are the most common magnetic phases on Earth and serve as important carriers of the paleomagnetic record (Buddington and Lindsley 1964; Lindsley 1991; Rohrbach et al. 2007). The magnetic, electrical, and thermodynamic properties of these minerals depend on the concentration and distribution of Fe and Ti among sites of different symmetry in the structure (Lindsley 1976). Two Fe-Ti oxide solid-solution series are relevant for magnetic studies—the titanomagnetite (TM) and the titanohematite-hemoilmenite series (Franke et al. 2007). TM is the cubic spinel series between the magnetite (Fe_3O_4) and ulvöspinel (Fe_2TiO_4) end-members. The general TM formula is $Fe_{3-x}Ti_xO_4$, where x is the mole fraction of the ulvöspinel component. Hereafter, TM compositions will be given as "TMx," for example TM60 for x = 0.6.

The Raman spectra of the end-members of the titanomagnetite solid solution, magnetite (deFaria et al. 1997; Degiorgi et al. 1987; Gasparov et al. 2000; Shebanova and Lazor 2003a, 2003c; Verble 1974), ulvöspinel, and of some intermediate Ti compositions (Wang et al. 2004) are available. However, a systematic study of the changes of the line positions and their relative intensities as Ti is substituted into magnetite does not appear to have been reported. Here, we describe a study on the Raman spectroscopy of the titanomagnetites to see whether variation in chemical bonding can be used for their identification. Raman spectroscopy is commonly used for characterization in chemistry and materials science because the vibrational information gathered is very specific for the chemical bonds in molecules. Moreover the most recent Raman microscopes have mapping capabilities that allow them to reveal the distribution of mineral phases with high spatial and spectral resolutions (Zinin et al. 2007). Raman spectroscopy can also be used as a tool to detect minerals remotely (Sharma et al. 2010). The proper identification of the Raman spectra of TM minerals may be of importance particularly now, when FeTi oxide were found in the Gusev crater on Mars (McSween et al. 2004). In the future, TM minerals may be identified using a remote Raman spectrometer.

The TM composition is an important parameter in studies on the magnetism of terrestrial and extraterrestrial materials. In planetary science applications, it has an additional advantage in that it can be measured remotely. In terrestrial work, Curie points are commonly used to determine the composition of these magnetic phases (Akimoto 1962). However, Curie points generally reflect bulk rock properties and do not provide insight for individual grains or intra-grain compositional variation in a sample. Determination of the composition of individual Fe-Ti oxide grains can also be made with electron microprobe techniques, electron backscatter diffraction in scanning electron microscopy (Franke et al. 2007), and X-ray diffraction (Madsen et al. 2009). However, all these techniques require special sample preparation and cannot be used in remote determinations of the Ti content of titanomagnetites.

We present results for the composition parameter x, defined by ($Fe_{3-x}Ti_xO_4$), with x = ~0.0, 0.2, 0.4, and 0.6, namely TM0, TM20, TM40, and TM60. The results from our systematic study were used to quantify the Ti content variations within and between titanomagnetite grains in a basaltic sample from the Hana volcano on Maui Island in the Hawaiian chain and in a melatroctolite sample from Cumberland, Rhode Island.

* E-mail: zinin@soest.hawaii.edu

0003-004X/11/0010–1537$05.00/DOI: 10.2138/am.2011.3745

MATERIALS AND METHODS

Natural magnetite from the Mount Givens pluton (California) was used for TM0 (Gilder and McNulty 1999). Other samples, TM20, TM40, and TM60, were prepared using the floating zone technique (Wanamaker and Moskowitz 1994). The Ti concentrations were verified by thermomagnetic analysis (Gilder and Le Goff 2008) as well as electron probe microanalysis (EPMA). Using the correspondence of Curie temperatures on heating to titanium concentrations (Akimoto 1962), the concentration of Ti in the TM samples was found to be $x = 0.19$ for TM20 specimen, $x = 0.39$ for TM40, and $x = 0.6$ for TM60 (Gilder and Le Goff 2005). Electron microprobe analysis of the TM samples was performed using a JEOL Hyperprobe JXA-8500F at the School of Ocean and Earth Science and Technology, University of Hawaii. The chemical compositions obtained from EPMA are presented in Table 1. As seen in Table 1, the EPMA technique provides a slightly different composition for the TM specimens: $x = 0.18$ for TM20 specimen; $x = 0.41$ for TM40; and $x = 0.64$ for TM60. In this report, we will use the concentration of Ti in TM measured by the EPMA techniques (Table 1) because this technique is accepted as standard for elemental composition measurements in mineralogy (Reed 2010).

The X-ray diffraction technique was used for the structure characterization of the TM specimens. Because some of the specimens were small (~60 μm), and high accuracy of the X-ray peak detection is required to estimate the effect of the Ti incorporation on the TM unit cell, the X-ray measurements were conducted at the GeoSoilEnviro-CARS, station 13ID-B [Advanced Photon Source (APS), Argonne National Laboratory (ANL)]. To measure X-ray spectra, samples were compressed into a small pellet inside a 150 μm hole in a stainless gasket. A diamond-anvil cell (DAC) was used to press the sample into the hole. The metal gasket serves as a holder to place the sample in the X-ray beam. Two sets of measurements were taken for TM0, TM20, TM40, and TM60. For the first set we did a 5×5 scan with 20 μm steps and the detector placed 250 mm away from the sample. For the second set we did a 3×3 scan with 25 μm steps and the detector placed 200 mm away from the sample. This second detector position yields lower resolution but allows the detection of X-rays diffracted by *d*-spacings between 1.07 and 0.88 Å. The spatial resolution of the 0.3344 Å X-ray beam is around 7 μm. X-ray pattern images were calibrated and transformed to 2D spectra with FIT2D V12.077 software, using an X-ray pattern obtained from CeO as a reference. To study the diffraction patterns, Grams/AI v8.0 was used for baseline correction and peak fitting to a mixture of Gaussian and Lorentzian shapes.

Raman spectra were collected for each sample using a WiTec Alpha300R confocal Raman microscope with an Nd-YAG green (532 nm) laser (Coherent Compass). For Raman spectra measurements, small, unpolished grains approximately 30 to 100 μm in size with different Ti concentrations were mounted on carbon tape attached to a glass slide. The experimental conditions were kept identical between samples to avoid any artifacts. The power of the laser beam at the sample surface was kept below 0.7 mW to avoid sample damage (deFaria et al. 1997; Shebanova and Lazor 2003b); neutral density filters were used to deliver a constant power of 675 μW. Consecutive replicate measurements were performed to ensure no photoalteration of the samples was induced during 532 nm excitation. All the spectra were acquired through a 50× objective, leading to a laser spot diameter around 2 μm. A grating of 600 g/mm centered on 2200 cm^{-1} was used, leading to the spectral window from 95 to 3700 cm^{-1}. The calibration of the spectrometer was verified before and after each session by acquiring Raman spectra of a standard silicon wafer. The silicon wafer is characterized by only one intense Raman band (520 cm^{-1}). However, it was checked against a cyclohexane standard to ensure that the potential shift in the calibration of the spectrometer is constant and does not depend on the wavenumber. Twelve to sixteen spectra per sample were analyzed with an integration time of 30 s (3×10 s). An average spectrum of 12–16 spectra was obtained for each sample. We subtracted the interfering signal and corrected for background aberrations using the Grams software package (Thermo Fisher Scientific, Inc.). Sixth-order polynomials were used for background correction. Peaks were fitted using mixed Gaussian and Lorentzian peak functions.

TABLE 1. Average composition of TM samples as determined by electron probe microanalysis

Oxide/element	TM20	TM40	TM60
TiO_2	6.16 (0.11)	14.02 (0.15)	22.53 (0.09)
Fe_2O_3	56.84 (0.26)	41.57 (0.30)	25.84 (0.17)
FeO	35.83 (0.11)	43.02 (0.19)	51.32 (0.13)
Total	98.83	98.61	99.69
Number of cations on the basis of 4 O atoms			
Ti	0.18	0.41	0.64
Fe^{3+}	1.66	1.21	0.74
Fe^{2+}	1.16	1.39	1.62

Note: Numbers in parentheses are estimated standard deviations.

To check the effect of Ti on the Raman spectra of natural samples, we studied a magnetite-rich melatrocolite sample from Cumberland (Rhode Island), which was kindly supplied by M.J. Rutherford, and a sample from the Hana Volcanics of Maui Island in the Hawaiian chain from E. Herrero-Bervera. A magnetite-rich melatroctolite, which crops out at the Iron Mine Hill in Cumberland, Rhode Island, consists primarily of olivine, titaniferous magnetite (to 32%), smaller amounts of plagioclase, and minor aluminum-rich spinel and ilmenite (Rutherford and Hermes 1984); it contains no pyroxene. Wadsworth introduced the name "cumberlandite" to describe this rock (Wadsworth 1984), however, following IUGS classification (Streckeisen 1973), the name "magnetite-rich melatroctolite" seems preferable. The only other known occurrence of a similar rock is from Taberg, Sweden, although generally similar assemblages are found in titaniferous magnetite deposits and associated anorthosites (Rutherford and Hermes 1984). The titanomagnetite grains contain pleonaste exsolution lamellae as well as ilmenite-rich lamellae formed by oxyexsolution; petrology and petrography are described in detail elsewhere (Rutherford and Hermes 1984). Titanomagnetite grains in a polished thin section of the sample (~15×6 mm) supplied by M.J. Rutherford were analyzed by EPMA and Raman microscopy.

Petrology and petrography of the sample from the Hana Volcanics of Maui Island (HKAM) specimen are described in detail elsewhere (Herrero-Bervera and Valet 2007). Briefly, the East Maui volcano is the youngest and largest of the two edifices of the island of Maui. Hana volcanism is the only example of rejuvenated volcanism in Hawaii that follows former rift zone structures. The rejuvenation stage Hana rocks are alkalic, although they tend to have lower SiO_2 content and are less differentiated. Carbon dating and geological evidence suggest that there have been at least five eruptions along the SW rift zone in the last 900 years. The location of the HKAM site on the Hana Volcanic can be found elsewhere (Herrero-Bervera and Valet 2007). The measurements were conducted on a single polished slide of a sample of HKAM.

RESULTS

The X-ray diffraction data indicate that all TM members have the cubic crystal structure (space group *Fd*3*m*) characteristic of the spinel group. The spinel group of minerals, with the general formula AB_2O_4, includes a large number of end-members with predominantly cubic crystal structure. The ideal spinel structure consists of a face-centered unit cell containing 32 O atoms arranged in a cubic close-packed framework. Eight cations occupy one-eighth of the tetrahedral sites, and 16 cations occupy half of the octahedral interstices within the oxygen framework (Sedler et al. 1994). Using the formula AB_2O_4, the spinels can be divided into "normal" and "inverse" types on the basis of the cation arrangements (Barth and Posnjak 1932). In a normal spinel, the A cations occupy only tetrahedral positions and the B cations only octahedral positions. In an inverse spinel, half of the B cations occupy the tetrahedral positions, whereas the other half of the B cations fills the octahedral positions together with the A cations. A perfect inverse spinel can thus be represented by the structural formula $^{IV}B^{VI}(AB)O_4$ (Sedler et al. 1994).

The titanomagnetite series has a general formula $A_xB_{2-x}O_4$, where A and B represent tetrahedrally coordinated cations and octahedrally coordinated cations, respectively. End-members of the titanium magnetite family, magnetite ($x = 0$) and ulvöspinel ($x = 1$), have the inverse spinel structure, with space group *Fd*3*m* (Barth and Posnjak 1932; Fleet 1981; Lindsley 1976; Wechsler et al. 1984). For the case of magnetite, the Fe^{3+} ion occupies the A sites, while B sites are occupid by Fe^{2+} and the remaining Fe^{3+} ions (Stacy and Banerjee 1974). As Ti substitution in magnetite proceeds, Ti^{4+} ions enter the B sites (Blasse 1964; Pearce et al. 2010). In the ulvöspinel, the Ti is octahedral and Fe^{2+} occupies both tetrahedral and octahedral sites (Wechsler et al. 1984). X-ray spectra of TM0, TM20, TM40, and TM60 after background

correction are illustrated in Figure 1. X-ray patterns of the TM series have a set of peaks similar to that of magnetite. The (*nkl*) assignment of the peaks can be found elsewhere (Sedler et al. 1994); see also JCPDS no. 11-0614, 19-0629, 34-0177). X-ray patterns associated with TM specimens were found to be uniform over the scan area, showing a pattern corresponding to a crystal with space group *Fd*3*m*. We found that some TM60 spectra show two additional and very weak peaks at 1.871 and 2.032 Å with intensities of <1% (Fig. 1). The origin of these two peaks is unknown. The (311) peaks (centered at 1.9272 Å for TM0) are very weak [less than 2% of the intensity of the main (133) peak] on the X-ray spectra of TM0, TM40, and TM60; however, it appears to be strong on the X-ray spectrum of TM20 with 11% of the intensity of the main (133) peak (Fig. 1). The reason for the enhancement intensity of the (311) peak on the spectrum of TM20 is unclear and has not been discussed in the literature. Distribution of the X-ray intensity on the diffraction images and optical images of the TM specimens are shown in Figure 2. Analysis of the X-ray diffraction images does not support a claim that synthesized specimens are single crystals (Gilder and Le Goff 2005). All the X-ray patterns contain rings and spots indicating that all the TM specimens are polycrystals with different degrees of crystallinity.

Parameters of the unit cell of TM specimens were determined by refinement software (Holland and Redfern 1997). The positions of the 14 main peaks of the X-ray pattern for the TM series were used for refinement purposes. The fitting to a face-centered cubic crystal lattice provides the following lattice parameters for the four different samples used in this study: TM0, $a = 8.4002(2)$; TM20, $a = 8.4109(4)$; TM40, $a = 8.4481(6)$; TM60, $a = 8.4832(2)$ Å. The value of the experimental error is shown in parentheses. The observed *d*-spacings corresponding to the magnetite crystal structure clearly shift toward wider spacings with the increase of Ti concentration (Fig. 3). The unit-cell parameter of the titanomagnetite series was found to have a strong correlation with Ti concentration (Bosi et al. 2008; O'Reilly 1984; Wechsler et al. 1984). The observed lattice parameters of the TM series are in a good agreement (Fig. 3) with experimental data published by Wechsler et al. (1984), which provides additional justification for the compositions of TM specimens measured with EPMA technique. Experimental data by Wechsler et al. (1984) shown in Figure 3 were with a third-order polynomial: $a = 8.3957 + 0.0688 \cdot x + 0.1957 \cdot x^2 - 0.1247 \cdot x^3$ ($r^2 = 0.9995$).

The Raman spectra of TM0, TM20, TM40, and TM60 before and after background correction are illustrated in Figures 4 and 5, respectively. Table 2 lists the major peak positions of

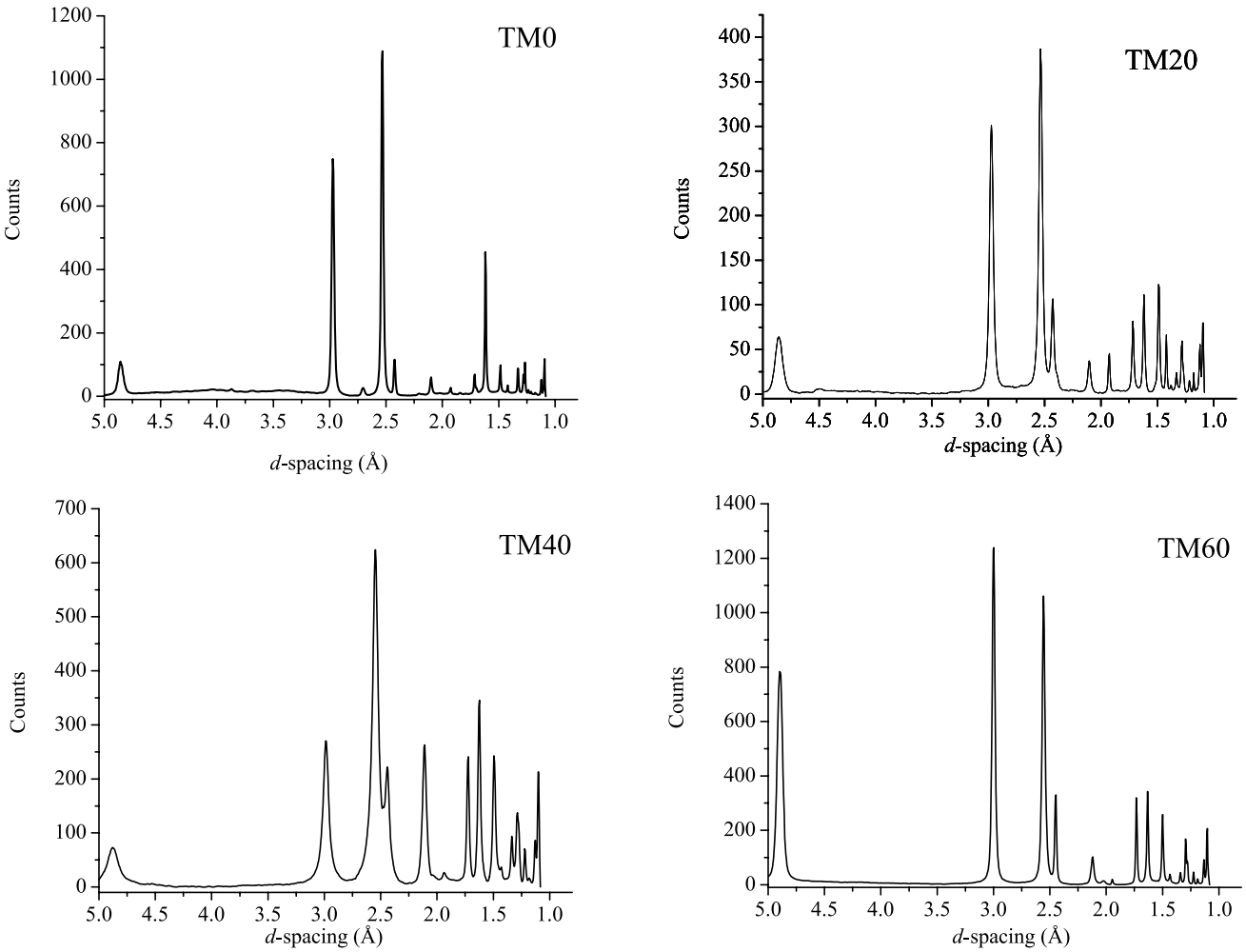

FIGURE 1. X-ray spectra of TM0, TM20, TM40, and TM60 specimens after background corrections.

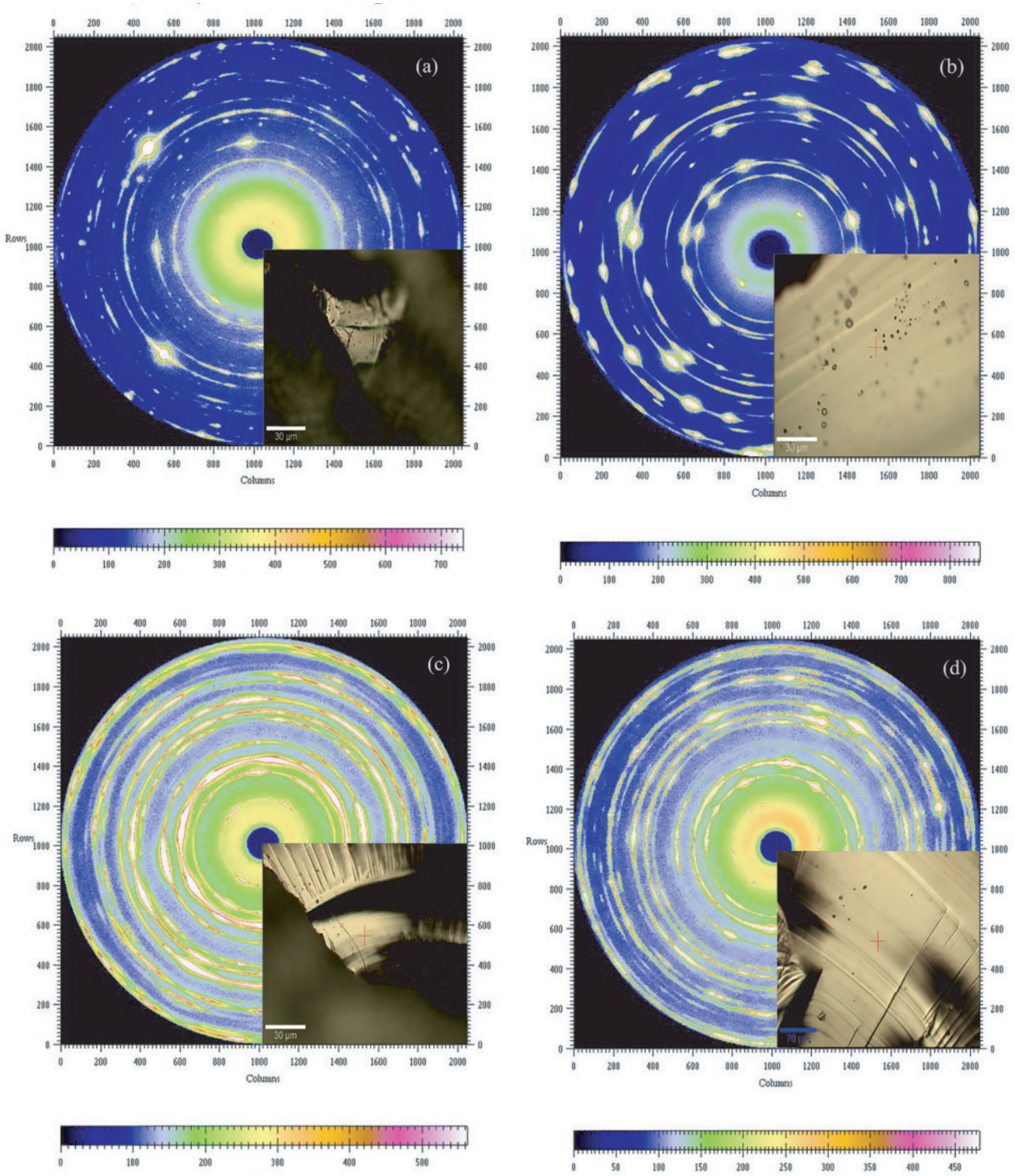

FIGURE 2. X-ray patterns of TM specimens: (**a**) TM0; (**b**) TM20; (**c**) TM40; (**d**) TM60. Inserts are optical images of the TM specimens taken with objective ×100 before Raman spectra measurements. (Color online.)

these samples and for magnetite and ulvöspinel from published works (Shebanova and Lazor 2003a; Wang et al. 2004). The five previously reported Raman peaks for spinel structure at ~190, 310, 460, 540, and 670 cm^{-1} were observed for TM40, and are discernible for TM60. A symmetry analysis and an assignment of magnetite phonon modes based on the spinel structure was made by Degiorgi et al. (1987), Gasparov et al. (2000), and Verble (1974). The theoretical analysis based on the factor-group approach predicts five Raman active bands: A_{1g}, E_g, and three T_{2g} (White and DeAngelis 1967). Above $T > 120$ K, magnetite has a

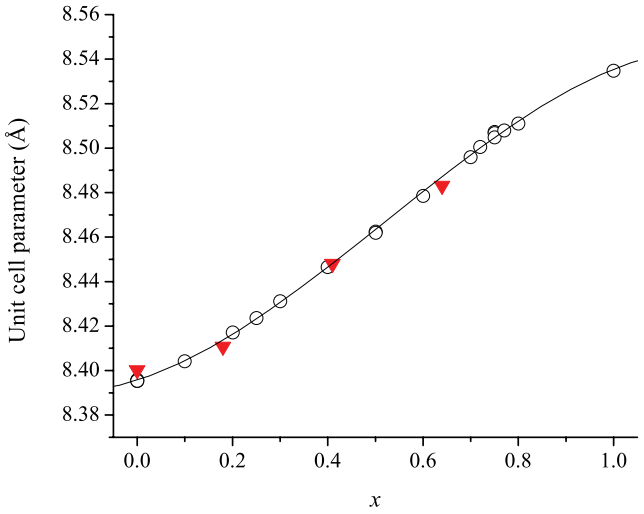

FIGURE 3. The variation of the unit-cell parameter *a* vs. concentration parameter *x* in $Fe_{3-x}Ti_xO_4$: solid triangles are unit-cell parameters measured in this research; open circles are experimental data from Wechsler et al. (1984). Solid line (S-shaped curve) is the cubic regression fitting of the data from Wechsler et al. (1984). Error bars are not shown in the Figure 3 because their sizes are smaller than those of the symbols (triangles). (Color online.)

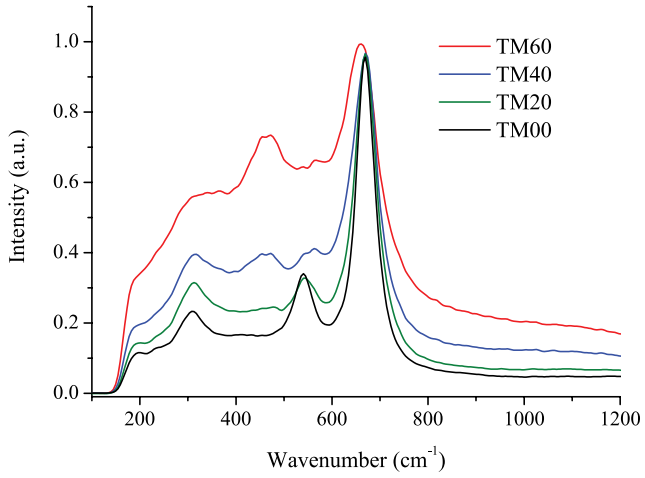

FIGURE 4. The average Raman spectra for each TM sample before background correction. (Color online.)

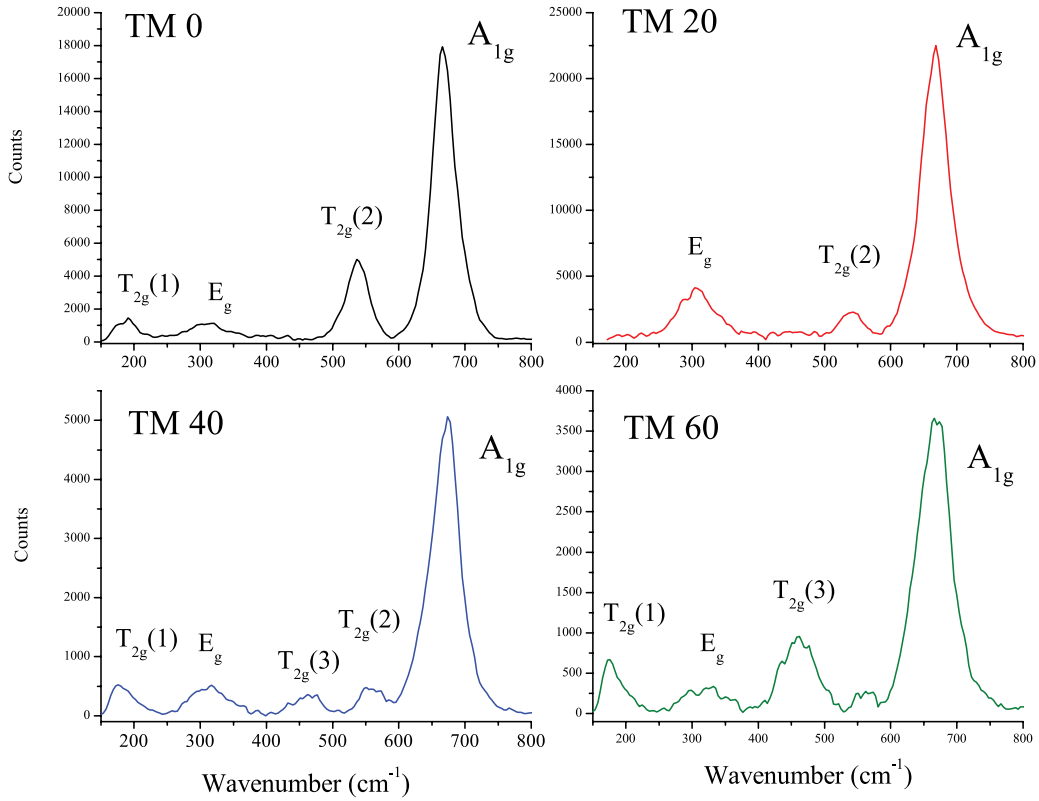

FIGURE 5. The average Raman spectra for each TM sample after background correction. (Color online.)

cubic-inverse-spinel structure belonging to the space group *Oh*7 (*Fd*3*m*). The full unit cell contains 56 atoms, but the smallest Bravais cell contains only 14 atoms (Gasparov et al. 2000); as a result, one should expect 42 vibrational modes. Group theory predicts the following modes:

$$A_{1g}+E_{g1}+T_{1g}+3T_{2g}+2A_{2u}+2E_u+5T_{1u}+2T_{2u}.$$

The T_{1g}, A_{2u}, E_u, and T_{2u} are silent. Thus, there are five Raman-active modes ($A_{1g}+E_{g1}+3T_{2g}$) and five infrared-active modes ($5T_{1u}$). At ambient conditions, the non-polarized spectrum of

TABLE 2. Raman mode frequencies (cm^{-1}) of TM samples in this study and other studies, and titanomagnetite in the melatroctolite sample (the position names A–D correspond to Fig. 7)

Sample	$T_{2g}(1)$	E_g	$T_{2g}(3)$	$T_{2g}(2)$	A_{1g}	Data from
TM100			495s	561w	679vs	1
TM60	184m	311vw	461s	569wv	662vs	2
TM40	183m	314m	457m	554vw	669vs	2
TM20	185wv	312s		544w	670vs	2
TM0	192w	308wv		540s	670vs	2
TM0	193w	306m		538s	668vs	3
A	184m	292vw	476s		669vs	2
B	182m	323w	469s		666vs	2
C	183m	320w	462w		667vs	2
D	182	324	452		673vs	2
Peak assigned by	3	3	3	3	4	

Notes: vs = very strong; s = strong; m = middle; w = weak; vw = very weak. References: 1 = Wang et al. (2004); 2 = this study; 3= Shebanova and Lazor (2003a); 4 = Verble (1974).

magnetite shows four out of the five theoretically predicted phonon bands at 193, 306, 538, and 668 cm^{-1} (Shebanova and Lazor 2003a). The Raman spectrum of our TM0 also contains the predicted A_{1g}, E_g, $T_{2g}(1)$, and $T_{2g}(2)$ modes at 670, 308, 192, and 540 cm^{-1}. The mode $T_{2g}(1)$ at 192 cm^{-1} is weak and was only reported by Gasparov et al. (2000) and Shebanova and Lazor (2003a). In this report, we use peak assignments for titanium magnetite suggested by Shebanova and Lazor (2003a): $T_{2g}(1)$, E_g, $T_{2g}(3)$, $T_{2g}(2)$, and A_{1g}. They suggest that "the location of the fifth, $T_{2g}(3)$, unobserved phonon mode, is inferred from spectra of other ferrites at 450–490 cm^{-1}."

DISCUSSION

Raman spectroscopy of synthetic titanomagnetites

It is natural to correlate the Ti concentration with the position of the Raman peaks of the TM specimens (Wang et al. 2004). Unfortunately, the Raman peaks of TM (Fig. 5) are anomalously broad (~30 cm^{-1}, see discussion in Verble 1974 and Wang et al. 2004), and incorporation of the Ti atoms into magnetite has no pronounced effect on the position of the Raman peaks so they cannot be used as a measure of Ti concentration (Table 2). As a rule, relative intensities of the Raman peaks are not used for quantitative determination of the component concentrations because of the high-fluorescent background. Only in ultraviolet Raman spectroscopy is the Raman peak area is proportional to cross sections of UV scattering by correspondent bonds (Zinin et al. 2010). The case of the visible Raman spectroscopy of titanium magnetite is an exception to the rule. Relative intensities of the Raman peaks can be used for estimation of the Ti concentration because the intensities of some Raman peaks change drastically as the concentration of Ti increases. As shown in Figures 4 and 5, the $T_{2g}(3)$ ~460 cm^{-1} peak is not detectable in TM0 and TM20, however, it becomes prominent in Raman spectra of TM40 and TM60 as the concentration of Ti increases. The increase in Ti concentration leads to the visible change of the peak intensities of $T_{2g}(3)$ mode. A slight (~2%) shift toward higher frequency was discernible for $T_{2g}(2)$ (540–569 cm^{-1}) with increasing Ti concentration. However, the change lies within experimental uncertainty; the position of the $T_{2g}(2)$ peak varies substantially even for pure magnetite (TM0)—534 cm^{-1} (deFaria et al. 1997) and 570 cm^{-1} (Graves et al. 1988).

Figure 6 illustrates the behavior of the relative intensities as a function of Ti concentration in the TM specimens. After background correction, the areas under the various Raman peaks were normalized to that of A_{1g} at ~670 cm^{-1}. The A_{1g} peak was chosen as the normalization factor because it was consistently the strongest peak for all samples and there was no discernible shift with Ti concentration change. Figure 6 shows that the relative intensity exhibits prominent changes with Ti concentration in titanomagnetite. The error bars in Figure 6 are the average standard deviations of the normalized intensity within the range of full-width at half maximum of each Raman peak for the obtained spectra. The most remarkable feature was the appearance of the $T_{2g}(3)$ peak centered at 457 cm^{-1} for TM40, which was absent for TM0 and TM20. The relative intensity of this peak increases sharply from TM40 to TM60. The $T_{2g}(2)$ peak centered at ~550 cm^{-1} in TM0, TM20, and TM40 gradually decreases as Ti concentration increases and appears to vanish at TM60. A less prominent gradual increase in relative intensity was observed in the $T_{2g}(1)$ mode at ~190 cm^{-1}. There was no noteworthy systematic dependence in intensity or peak position shift for the E_g peak at ~310 cm^{-1}. For $x > 0.2$, a polynomial fit of the relative intensity of the $T_{2g}(3)$ and A_{1g} peaks [$I_{T2g(3)}/I_{A1g}$] has the quadratic form

$$I_{T2g(3)}/I_{A1g} = -0.016 + 0.022 \times x + 0.491 \times x^2. \quad (1)$$

The relative intensity of the $T_{2g}(2)$ peak as a function the Ti concentration was fitted via an exponential relationship for $0 < x < 1$:

$$I_{T2g(2)}/I_{A1g} = 0.1254\ e^{-1.7113x}. \quad (2)$$

Intensities of the Raman peaks for ulvöspinel ($x = 1$) were deduced from Raman spectra published by Wang et al. (2004). The spectra were scanned, digitized, and the relative intensity of the Raman peaks deduced. The behavior of the Raman peak intensities is in agreement with the Wang et al. (2004) results.

The behavior of the intensity of the $T_{2g}(3)$ is not a monotonic function of titanium concentration x: up to below $x = 0.2$, peak $T_{2g}(3)$ is not detectable; above $x > 0.2$, the intensity of the $T_{2g}(3)$ peak gradually increases as the concentration of Ti increases. The unusual behavior of the intensity of the $T_{2g}(3)$ peak is certainly related to the distribution of the Fe and Ti cations in the spinel structure. Several models have been proposed for cation distribution in the titanomagnetite solid-solution series, particularly regarding Fe^{2+} and Fe^{3+} ions (Akimoto 1954; Kakol et al. 1991; O'Reilly and Banerjee 1965; Pearce et al. 2010; Wechsler et

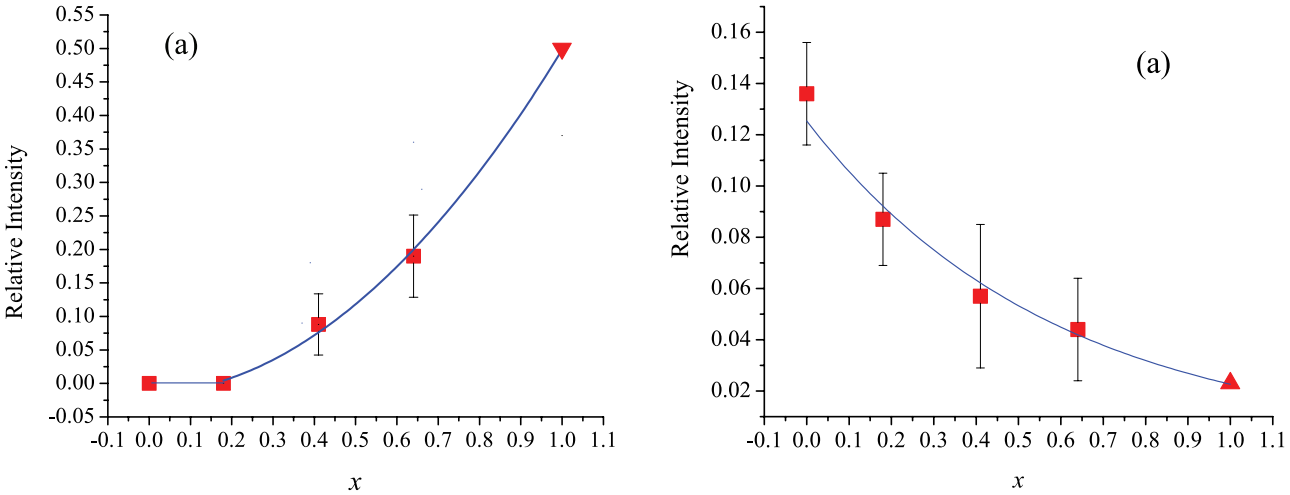

FIGURE 6. Plots of relative intensities vs. parameter *x* (obtained by electron probe microanalysis) for TM: (**a**) $I_{T2g(3)}/I_{A1g}$; (**b**) $I_{T2g(2)}/I_{A1g}$. Solid squares are results on measurements obtained in this study, solid triangles are results deduced from Wang et al. (2004). The curves are fit using Equations 1 and 2 for **a** and **b**, respectively. (Color online.)

al. 1984). One model suggests that Fe^{2+} ions first enter B sites with increasing Ti content and start to enter A sites at x = ~0.2 (Kakol et al. 1991). The electron hopping between Fe^{2+} and Fe^{3+} ions in B sites in magnetite causes a polaron conduction at room temperature (Verwey et al. 1947). It decreases as Ti substitution increases, whereas the Jahn-Teller distortion occurs as a result of Fe^{2+} occupancy in the A sites above x = ~0.2 (Kakol et al. 1991). These changes in cation occupancy with increasing Ti concentration affect the magnetic and electrical properties of titanomagnetite (O'Reilly 1994; Pearce et al. 2010). Therefore, the appearance of the $T_{2g}(3)$ modes (Fig. 5) and behavior of the intensity of this band (Fig. 6) are linked to the incorporation of Fe^{2+} in tetrahedral sites.

To explain the unusual behavior of the $T_{2g}(3)$ mode, we use Raman mode assignment, based on a group-theoretical analysis of the long wavelength phonons of magnetite developed by Verble (1974). According to Verble, Raman bands for the spinel structure were associated with the normal mode motions of four oxygen anions and Fe cations in each A site tetrahedron (Verble 1974). The atoms from the B site do not participate in the Raman active vibrations. Group-theoretical and lattice-vibration analyses based on the quasimolecular description of the spinel structure have led to the following description of normal mode motions of the FeO_4 tetrahedron (Verble 1974): A_{1g}, symmetric stretch of oxygen atoms along Fe-O bonds; E_g and $T_{2g}(3)$, symmetric and asymmetric bends of oxygen with respect to Fe, respectively; $T_{2g}(2)$, asymmetric stretch of Fe and O; $T_{2g}(1)$, translatory movement of the whole FeO_4 (Shebanova and Lazor 2003a). Such an assignment together with the Kakol et al. (1991) model of the Fe site occupancy provide a simple explanation of the Raman spectra in the titanomagnetite series. The $T_{2g}(3)$ mode is associated with symmetric and asymmetric bends of oxygen with respect to Fe and, therefore, its position is not directly dependent on the concentration of the Ti, which incorporates into the octahedral site. Incorporation of the Fe^{2+} in the tetrahedral site changes charge distribution in the tetrahedral site. Such redistribution of the charge can lead to an increase of the scattering cross section of the Raman $T_{2g}(3)$ band. Behavior of the peak $T_{2g}(3)$ intensity agrees well with the Kakol et al. (1991) model. According to this model, Fe^{2+} cations start occupying the tetrahedral site only at compositions of $x \geq 0.2$ (Kakol et al. 1991), in the same composition range where $T_{2g}(3)$ peaks become prominent.

As we can see from the Table 2, there is a change in the position of the $T_{2g}(3)$ as Ti concentration increases. The frequency of the Raman peak increases by four wavenumbers as concentration increases from 40 to 60%, and its increase is nearly 34 cm^{-1} when Ti concentration increases from 60 to 100% (Table 2). Such behavior of the $T_{2g}(3)$ Raman peak as a function of Ti concentration, x, correlates well with the behavior of the $I_{T2g(3)}/I_{A1g}$ ratio: its increase is more prominent as x approaches 1 (Fig. 6a). However, the anomalous broadness (~30 cm^{-1}, see discussion in Verble 1974; Wang et al. 2004) of Raman peaks of TM specimens does not allow us to make an unambiguous conclusion whether this position shift is characteristic of Ti concentration.

The relative intensity of the $T_{2g}(2)$ peak decreases gradually as the concentration of Ti increases. Looking at the monotonous behavior of the intensity of the $T_{2g}(2)$ as a function of x, one can infer that such behavior is determined by the vibration of the Ti atoms in the octahedral site (B site): an increase in the Ti concentration in the B site leads to the gradual decrease in the intensity of the $T_{2g}(2)$ (Fig. 6b). Wang et al. (2004) suggested that "$Ti^{4+}O_6$ octahedra should be the major producer of the main Raman peak of ulvöspinel." However, available experimental data does not allow us to provide an unambiguous answer as to whether Ti atoms in the octahedral sites are involved in the Raman active vibrations. Comparison of the behavior of the intensity of the $T_{2g}(2)$ peak with site occupancy for tetrahedral and octahedral Fe sites leads us to a conclusion that the intensity of the $T_{2g}(2)$ as a function of x correlates also with the behavior of tetrahedral Fe^{3+} and octahedral Fe^{3+} sites within the Kakol's model [see also Pearce et al. (2010)]. Moreover, theoretical simulations of the active Raman modes (Chamritski and Burns 2005; Verble 1974) suggested that atom vibrations associated with Raman mode centered at 540 cm^{-1} did not involve atoms

from the B (octahedral) site. A rigorous theoretical modeling of the Raman active modes of the TM is required to provide an unambiguous interpretation of the behavior of the $T_{2g}(2)$ as a function of Ti concentration.

The behavior of the peak intensities shown in Figure 6 can be used to estimate ~Ti concentrations in titanomagnetites. Indeed, the behavior of the relative intensity of the $T_{2g}(3)/A_{1g}$ peak [$I_{T2g(3)/A1g}$] is a good indicator of the Ti concentration for $x > 0.2$. On the other hand, the Raman peak for the $T_{2g}(2)$ mode gradually diminishes as Ti increases and nearly disappears at x = ~0.6. Combining the two relative intensities provides a potentially sensitive indicator of Ti content.

Raman spectroscopy of melatroctolite from Rhode Island

The analysis focused on the ubiquitous Fe-Ti compositional gradation within the exsolved titanomagnetite grain host. Compositional variations are observed in reflected light photomicrographs as a transition in color from darker regions surrounding ilmenite lamellae to interstitial lighter regions (Fig. 7a). The compositions of the four positions (A–D) shown in Figure 7a obtained by EPMA are listed in Table 3. Raman spectra taken at approximately the same position as those for EPMA are shown in Figures 7a–7b and Table 3. Qualitatively, the changes in spectra with increasing Ti compare well to that of our TM samples described above, especially if we consider the higher variations in intensity with increasing Ti (Fig. 6) and slight offsets of the spots analyzed by EPMA and Raman microscope (Fig. 7a). Using the equations obtained from the TM samples in the previous section, we find x values for the analyzed spots (Table 3). The concentration of Ti obtained from EPMA and Raman measurements is only in a good agreement at point D where the parameter x is around 0.2. The discrepancies are higher for high concentrations of Ti, particularly for $x > 0.6$, indicating that accurate calibration of the Raman intensity curves should be conducted in that area. We should also note that minor elements that exist in this natural titanomagnetite, such as Al and Mg, could cause non-negligible effects on Raman spectra. Although the effect is suspected to be similar to Ti substitution because of their preference to enter octahedral sites over tetrahedral sites (Richards et al. 1973), further investigation will be required to gain a fuller understanding of the titanomagnetite Raman spectra of natural samples with non-negligible amounts of minor elements.

Raman spectroscopy of HKAM sample from the Hana Volcanics

Raman spectra were taken from 18 grains. Eleven grains have a strong $T_{2g}(3)$ peak but a weak or not detectable $T_{2g}(2)$ peak, indicating that all these grains contain Ti. Figure 8 shows the optical image (Fig. 8a) and Raman spectrum (Fig. 8b) of one of such a grain from the HKAM specimen. The Raman spectrum was taken within the large titanomagnetite grain at the point marked by a red cross. We found that the composition is relatively constant within the grain, as Raman spectra were also taken at several other spots. Four grains have no $T_{2g}(3)$ peak, but do have $T_{2g}(2)$, indicating that the Ti concentration is close to 0 in these grains (Shebanova and Lazor 2003a). An optical image and Raman spectrum of one such grain is shown in Figure 9. Three out of eighteen grains from HKAM have peaks characteristic of hematite (Fig. 10) (deFaria et al. 1997). The Raman spectra of the

TABLE 3. Composition of titanomagnetite in the melatroctolite sample as determined by EPMA

Oxide/element	A	B	C	D
TiO_2	23.68	23.08	13.42	12.84
Al_2O_3	3.93	3.63	2.98	2.30
V_2O_3	0.36	0.43	0.73	0.75
Fe_2O_3	17.49	19.20	36.96	39.44
FeO	49.88	49.49	41.00	40.71
MnO	0.39	0.41	0.26	0.23
MgO	1.78	1.72	1.14	1.08
Total	95.80	96.08	92.89	93.45
Number of cations on the basis of 4 oxygen atoms				
Ti (EPMA)	0.66 (0.74)	0.64 (0.71)	0.39 (0.42)	0.37 (0.39)
Ti (Raman)	0.76	0.85	0.61	0.44
Al	0.17	0.16	0.13	0.10
V^{3+}	0.01	0.01	0.02	0.02
Fe^{3+}	0.49	0.54	1.07	1.13
Fe^{2+}	1.55	1.54	1.31	1.30
Mn^{2+}	0.01	0.01	0.01	0.01
Mg	0.10	0.10	0.07	0.06

Notes: Chromium was measured but is not listed because it was under detection level. The columns labeled A–D correspond to those in Figure 7. The number of cations for Ti is from EPMA and Raman spectroscopy. For EPMA, the values in parentheses are for the case in which other minor elements are disregarded in a pure titanomagnetite system. For Raman spectroscopy, the values were obtained by using Equation 1 for A–C. The relative error of the EPMA measurements of oxide concentrations at each point should not exceed 1% as estimated from repeated EPMA measurements of the Smithsonian standards: magnetite (USNM 114887) and ilmenite (USNM 96189). Description of the Smithsonian standards, magnetite and ilmenite, can be found elsewhere (Jarosewich et al. 1980).

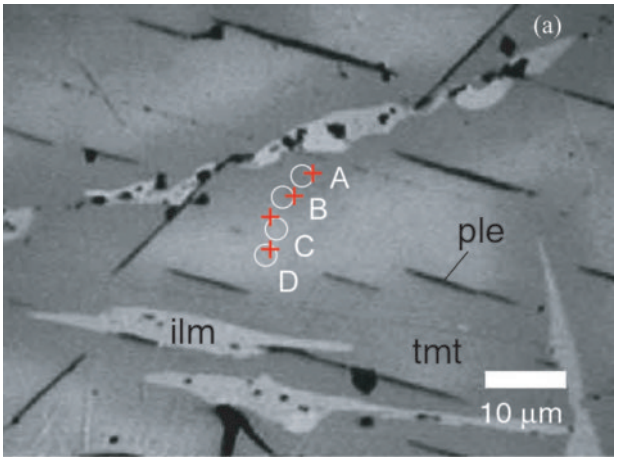

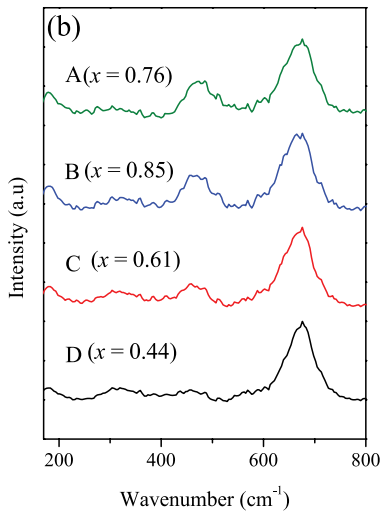

◀**FIGURE 7.** (**a**) A reflected light image of the region within a titanomagnetite grain in melatroctolite sample analyzed by electron probe microanalyzer (EPMA) and Raman spectroscopy: ilm = ilmenite; tmt = titanomagnetite; ple = pleonaste. Circles are spots analyzed by EPMA and crosses are spots analyzed by Raman. (**b**) Raman spectra of the four different spots shown in **a**. The x values were found using Equations 1 and 2. For A–C, Equation 2 was not applicable because the peak $T_{2g}(2)$ was not discernible. (Color online.)

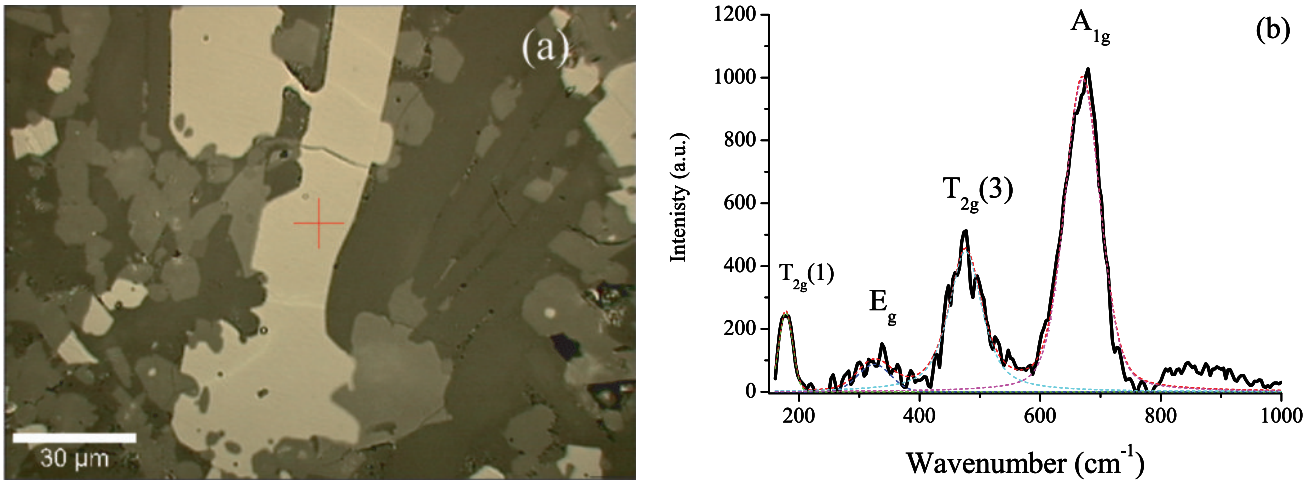

FIGURE 8. Optical image (**a**) and Raman spectrum (**b**) after background subtraction of a grain in a Hana basalt (HKAM) specimen: $Fe_{3-x}Ti_xO_4$; $x = \sim 0.6$. (Color online.)

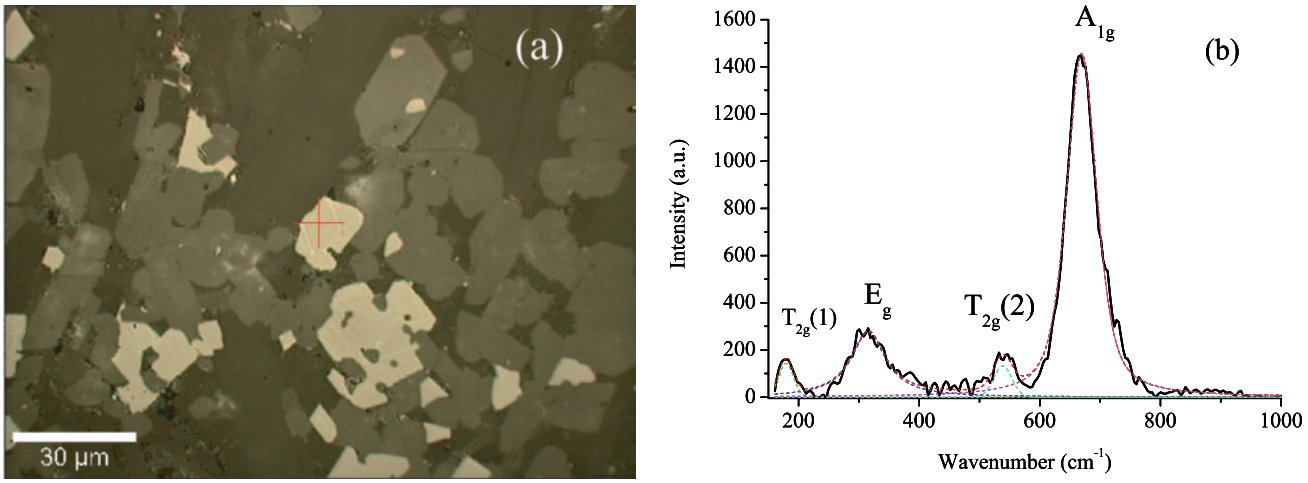

FIGURE 9. Optical image (**a**) and Raman spectrum (**b**) after background subtraction of a grain in a Hana basalt (HKAM) specimen: $Fe_{3-x}Ti_xO_4$; $x = \sim 0$; i.e., pure magnetite Fe_3O_4. (Color online.)

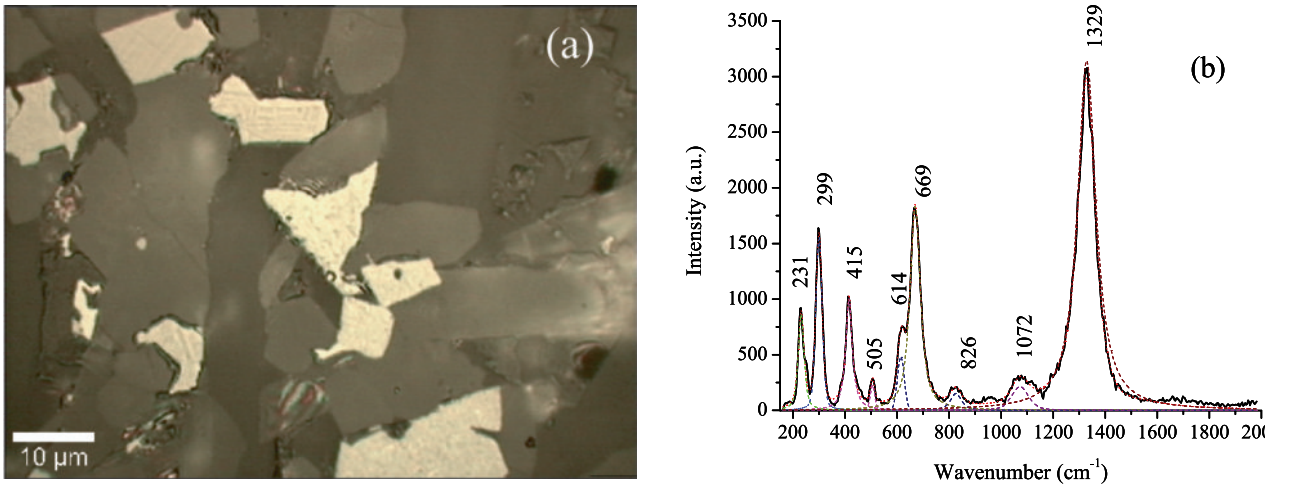

FIGURE 10. Optical image (**a**) and Raman spectrum (**b**) after background subtraction of a grain in a Hana basalt (HKAM) specimen: α-Fe_2O_3 hematite. (Color online.)

HKAM sample demonstrated that it contained numerous Ti-rich titanomagnetite grains with additional subsidiary magnetite and hematite. Although the presence of hematite could have been readily detected by optical microscopy, the homogeneity of Ti content between and within titanomagnetite grains could not have been so readily determined without Raman spectroscopy.

ACKNOWLEDGMENTS

L. Tatsumi-Petrochilos and M. Fuller received financial support from NSF Grant EAR-0609577, and S. Gilder from DFG Grant STA 1026/2-1. We thank M.J. Rutherford for the polished section from Cumberland (Rhode Island). We also thank O.K. Neill and E. Hellebrand for EPMA assistance. A portion of this work was performed at GSECARS (Sector 13), Advanced Photon Source (APS), Argonne National Laboratory. APS is supported by DOE-BES, under Contract no. DE-AC02-06CH11357.

REFERENCES CITED

Akimoto, S. (1954) Thermo-magnetic study of ferromagnetic minerals contained in igneous rocks. Journal of Geomagnetism and Geoelectricity, 6, 1–14.

——— (1962) Magnetic properties of FeO-Fe_2O_3-TiO_2 system as a basis of rock magnetism. Journal of the Physical Society of Japan, 17 (Suppl. B-1), 706–710.

Barth, T.F.W. and Posnjak, E. (1932) Spinel structures: with and without variate atom equipoints. Zeitschrift für Kristallographie, A, 82, 325–341.

Blasse, G. (1964) Crystal chemistry and some magnetic properties of mixed metal oxides with spinel structure. Philips Research Reports, Supplement 3, 1–139.

Bosi, F., Halenius, U., and Skogby, H. (2008) Stoichiometry of synthetic ulvospinel single crystals. American Mineralogist, 93, 1312–1316.

Buddington, A.F. and Lindsley, D.H. (1964) Iron-titanium oxide minerals and synthetic equivalents. Journal of Petrology, 5, 310–357.

Chamritski, I. and Burns, G. (2005) Infrared- and Raman-active phonons of magnetite, maghemite, and hematite: A computer simulation and spectroscopic study. Journal of Physical Chemistry B, 109, 4965–4968.

deFaria, D.L.A., Silva, S.V., and deOliveira, M.T. (1997) Raman microspectroscopy of some iron oxides and oxyhydroxides. Journal of Raman Spectroscopy, 28, 873–878.

Degiorgi, L., Blatter-Merke, I., and Wachter, P. (1987) Magnetite: Phonon modes and the Verwey transition. Physical Review B, 35, 5421.

Fleet, M.E. (1981) The structure of Magnetite. Acta Crystallographica, B37, 917–920.

Franke, C., Pennock, G.M., Drury, M.R., Engelmann, R., Lattard, D., Garming, J.F.L., von Dobeneck, T., and Dekkers, M.J. (2007) Identification of magnetic Fe-Ti oxides in marine sediments by electron backscatter diffraction in scanning electron microscopy. Geophysical Journal International, 170, 545–555.

Gasparov, L.V., Tanner, D.B., Romero, D.B., Berger, H., Margaritondo, G., and Forro, L. (2000) Infrared and Raman studies of the Verwey transition in magnetite. Physical Review B, 62, 7939–7944.

Gilder, S. and Le Goff, M. (2005) Pressure dependence on the magnetic properties of titanomagnetite using the reversible susceptibility method. In J.H. Chen, Y.B. Wang, T.S. Duffy, G.Y. Shen, and L. Dobrzhinetskaya, Eds., Advances in High-Pressure Technology for Geophysical Applications, p. 315–335. Elsevier, Amsterdam.

——— (2008) Systematic pressure enhancement of titanomagnetite magnetization. Geophysical Research Letters, 35, L10302.

Gilder, S. and McNulty, B.A. (1999) Tectonic exhumation and tilting of the Mount Givens pluton, central Sierra Nevada, California. Geology, 27, 919–922.

Graves, P.R., Johnston, C., and Campaniello, J.J. (1988) Raman scattering in spinel structure ferrites. Materials Research Bulletin, 23, 1651–1660.

Herrero-Bervera, E. and Valet, J.P. (2007) Holocene paleosecular variation from dated lava flows on Maui (Hawaii). Physics of the Earth and Planetary Interiors, 161, 267–280.

Holland, T.J.B. and Redfern, S.A.T. (1997) Unit cell refinement from powder diffraction data: the use of regression diagnostics. Mineralogical Magazine, 61, 65–77.

Jarosewich, E., Nelen, J.A., and Norberg, J.A. (1980) Reference samples for electron microprobe analysis. Geostandards Newsletter, 4, 43–47.

Kakol, Z., Sabol, J., and Honig, J.M. (1991) Cation distribution and magnetic properties of titanomagnetites $Fe_{3-x}Ti_xO_4$, $0 \le x < 1$. Physical Review B., 43, 649–654.

Lindsley, D.H. (1976) The crystal chemistry and structure of oxide minerals as exemplified by the Fe-Ti oxides. In D. Rumble III, Ed., Oxide Minerals, 3, p. L1–L60. Reviews in Mineralogy, Mineralogical Society of America, Chantilly, Virginia.

——— (1991) Experimental studies of oxide minerals. In D.H. Lindsley, Ed., Oxide Minerals: Petrologic and magnetic significance, 25, p. 69–106. Reviews in Mineralogy, Mineralogical Society of America, Chantilly, Virginia.

Madsen, M.B., Goetz, W., Bertelsen, P., Binau, C.S., Folkmann, F., Gunnlaugsson, H.P., Hjøllum, J.í., Hviid, S.F., Jensen, J., Kinch, K.M., and others. (2009) Overview of the magnetic properties experiments on the Mars Exploration Rovers. Journal of Geophysical Research-Planets, 114, E06S90.

McSween, H.Y., Arvidson, R.E., Bell, J.F., Blaney, D., Cabrol, N.A., Christensen, P.R., Clark, B.C., Crisp, J.A., Crumpler, L.S., Des Marais, D.J., and others. (2004) Basaltic rocks analyzed by the Spirit rover in Gusev Crater. Science, 305, 842–845.

O'Reilly, W. (1984) Rock and Mineral Magnetism. Blackie, Glasgow.

——— (1994) Magnetic recording in nature—The medium, the mechanism and the message. Journal of Magnetism and Magnetic Materials, 137, 167–185.

O'Reilly, W. and Banerjee, S.K. (1965) Cation distribution in titanomagnetites $(1–x)Fe_3O_4 – xFe_2TiO_4$. Physics Letters, 17, 237–238.

Pearce, C.I., Henderson, C.M.B., Telling, N.D., Pattrick, R.A.D., Charnock, J.M., Coker, V.S., Arenholz, E., Tuna, F., and van der Laan, G. (2010) Fe site occupancy in magnetite-ulvospinel solid solutions: A new approach using X-ray magnetic circular dichroism. American Mineralogist, 95, 425–439.

Reed, S.J.B. (2010) Electron Microprobe Analysis and Scanning Electron Microscopy in Geology, 2nd edition. Cambridge University Press, U.K.

Richards, J.C.W., O'Donovan, J.B., Hauptmann, Z., Reilly, W.O., and Creer, K.M. (1973) A magnetic study of titanomagnetite substituted by magnesium and aluminium. Physics of the Earth and Planetary Interiors, 7, 437–444.

Rohrbach, A., Ballhaus, C., Golla-Schindler, U., Ulmer, P., Kamenetsky, V.S., and Kuzmin, D.V. (2007) Metal saturation in the upper mantle. Nature, 449, 456–458.

Rutherford, M.J. and Hermes, D.O. (1984) Melatroctolite-anorthositic gabbro complex, Cumberland, Rhode Island: Petrology, origin, and regional setting. GSA Bulletin, 95, 844–854.

Sedler, I.K., Feenstra, A., and Peters, T. (1994) An X-ray powder diffraction study of synthetic $(Fe,Mn)_2Ti_4$ spinel. European Journal of Mineralogy, 6, 873–885.

Sharma, S.K., Misra, A.K., Clegg, S.M., Barefield, J.E., Wiens, R.C., and Acosta, T. (2010) Time-resolved remote Raman study of minerals under supercritical CO2 and high temperatures relevant to Venus exploration. Philosophical transactions of the Royal Society of London. Series A Mathematical, Physical and Engineering Sciences, 368, 3167–3191.

Shebanova, O.N. and Lazor, P. (2003a) Raman spectroscopic study of magnetite ($FeFe_2O_4$): a new assignment for the vibrational spectrum. Journal of Solid State Chemistry, 174, 424–430.

——— (2003b) Raman study of magnetite (Fe_3O_4): laser-induced thermal effects and oxidation. Journal of Raman Spectroscopy, 34, 845–852.

——— (2003c) Vibrational modeling of the thermodynamic properties of magnetite (Fe_3O_4) at high pressure from Raman spectroscopic study. Journal of Chemical Physics, 119, 6100–6110.

Stacy, F.D. and Banerjee, S.K. (1974) The Physical Principles of Rock Magnetism. Elsevier Science, New York.

Streckeisen, A.L. (1973) Plutonic rocks: Classification and nomeclature recommended by the I.U.G.S. subcommittee on the systematic of ingenious rocks. Geotimes, 18, 26–30.

Verble, J.L. (1974) Temperature-dependent light-scattering studies of the Verwey transition and electronic disorder in magnetite. Physical Review B, 9, 5236.

Verwey, E.J., Haayman, P.W., and Romeijn, F.C. (1947) Physical properties and cation arrangement of oxides with spinel structures II. electronic conductivity. Journal of Chemical Physics, 15, 181.

Wadsworth, M.E. (1984) Lithological Studies. Harvard College Museum of Comparative Zoology Memoir.

Wanamaker, B.J. and Moskowitz, B.M. (1994) Effect of nonstoichiometry on the magnetic and electrical properties of synthetic single crystal $Fe_{2.4}Ti_{0.6}O_4$. Geophysical Research Letters, 21, 983–986.

Wang, A., Kuebler, K.E., Jolliff, B.L., and Haskin, L.A. (2004) Raman spectroscopy of Fe-Ti-Cr-oxides, case study: Martian meteorite EETA79001. American Mineralogist, 89, 665–680.

Wechsler, B.A., Lindsley, D.H., and Prewitt, C.T. (1984) Crystal structure and cation distribution in titanomagantites ($Fe_{3-x}Ti_xO_4$). American Mineralogist, 69, 754–770.

White, W.B. and DeAngelis, B.A. (1967) Interpretation of the vibrational spectra of spinels. Spectrochimica Acta Part A: Molecular Spectroscopy, 23, 985–995.

Zinin, P.V., Huss, G.R., Sharma, S.K., Krot, A.N., and Bonal, L. (2007) Raman spectroscopic study of Roosevelt County (RC) 075 chondrite. 8th Lunar and Planetary Science Conference, Lunar and Planetary Science XXXVIII, League City, Texas. LPI Contribution no. 1338, p. 2223.

Zinin, P.V., Misra, A., Kamemoto, L., Yu, Q., Hu, N., and Sharma, S.K. (2010) Visible, near-infrared, and ultraviolet laser-excited Raman spectroscopy of the monocytes/macrophages (U937) cells. Journal of Raman Spectroscopy, 41, 268–274.

MANUSCRIPT RECEIVED NOVEMBER 23, 2010
MANUSCRIPT ACCEPTED MAY 9, 2011
MANUSCRIPT HANDLED BY AARON CELESTIAN